DOI: 10.1002/ ((please add manuscript number))
Article type: Full Paper

Atomic-Scale Observation of Irradiation-Induced Surface Oxidation by In-Situ Transmission Electron Microscopy

Xing Huang, Travis Jones, Hua Fan, and Marc-Georg Willinger**

Dr. X. Huang, Dr. T. Jones, Dr. H. Fan, Dr. M. G. Willinger

Department of Inorganic Chemistry, Fritz-Haber Institute of Max-Planck Society, Faradayweg 4-6, 14195, Berlin, Germany.

Email: xinghuang0214@mail.ipc.ac.cn; xinghuang@fhi-berlin.mpg.de (X. Huang); willinger@fhi-berlin.mpg.de (M. G. Willinger)

Keywords: in-situ TEM, EELS, electron-beam irradiation, structural transition, sulfur vancancy

Irradiation of materials with high energy particles can induce structural transitions or trigger chemical reactions. Understanding the underlying mechanism for irradiation-induced phenomena is of both scientific and technical importance. Here, we use CdS nanoribbons as a model system to study structural and chemical evolution under electron-beam irradiation by in-situ transmission electron microscopy (TEM). Real-time imaging clearly shows that upon irradiation, CdS is transformed to CdO with formation of orientation dependent relationships at surface. The structural transition can always be triggered with a dose rate beyond 601 e/Å^{2}s in this system. A lower dose rate instead leads to the deposition of an amorphous carbon layer on the surface. Based on real-time observations and DFT calculations, we propose a mechanism for the oxidation of CdS to CdO. It is essentially a thermodynamically driven process that is mediated by the formation of sulfur vacancies due to the electron-beam irradiation. We also demonstrate that the surface oxidation can be suppressed by pre-depositing a conductive carbon layer on the CdS surface. The carbon coating can effectively reduce the rate of sulfur vacancy creation, thus decreasing defect mediated oxidation. In

addition, it isolates the active oxygen radicals from the ribbon, blocking the pathway for oxygen diffusion.

1. Introduction

Irradiation resistance is a critical property of materials that are used in appications such as aerospace[1], nuclear energy[2], and some other industrial applications[3]. Irradiation of materials with high energy particles, such as electrons and neutrons, can easily displace atoms from their equilibrium positions in the crystal lattice and create point defects[4-6] (vacancies, interstitials). Consecutive irradiation further drives the evolution of atomic defects into microstructural flaws, forming for instance voids[4], dislocation loops[7] or interstitial precipitation[8]. In some cases, phase transition and chemical reactions can also be triggered as a result of irradiation[9]. Since materials' physical and chemical properties are strongly connected to their crystal structutre and chemical composition[10, 11], study of irradiation-induced structural and chemical evolutions is of both scientific and technical importance[12, 13], especially for those materials with irradiation-related applications.

The transmission electron microscope represents an ideal tool for such studies[14, 15]. It can deliver electrons with kinetic energies ranging from 20 keV to 1.5 MeV[5], sufficient to cause atomic defects or structural transitions. More importantly, it allows real-time imaging at the atomic-scale[16-18], which may advance our understanding of irradiation-induced effects at that same level. Many successful examples have been demonstrated through irradiation study by TEM. For instance, L. Yao et al., demonstrated that an electron beam can lead to a controlled perovskite-brownmillerite phase transition in epitaxial $La_{2/3}Sr_{1/3}MnO_3$ films, which is driven by an incessant ordering of electron-beam induced oxygen vacancies[9]. J. Kotakoski et al., reported an electron-beam-induced transformation of graphene into a two-dimensional coherent amorphous membrane composed of sp^2-hybridized carbon atoms, providing new insights into the bonding behavior and dynamics of defects in graphene[13]. Those studies

imply that the irradiation can be benefical, which could serve as a powerful tool to tailor the structure of materials[19].

As an important semiconductor compound of II-VI group, nanostructured CdS, such as nanowires[20] and nanoribbons[21], has received tremendous attention in the past two decades due to its fascinating properties[22, 23]. However, with most previous efforts dedicated to exploring their possible uses in electronic[24], photocatalytic[25] and energy-related applications[26], few studies have been devoted to investigating irradiation-induced effects. As far as we know, a detailed observation of the process and an atomic-scale mechanistic understanding are still missing. Moreover, an operational method that can suppress the irradiation effects of CdS nanostructures has yet to be demonstrated. A systematic investigation of beam induced transformation will be beneficial for the design of CdS-based devices working under irradiation environments, and is thus of high interest. Using CdS nanoribbons as a model system we provide an experimental basis for understanding electron beam induced structural evolution. Real-time atomic-scale imaging by in-situ TEM provides detailed insight on the electron beam induced transition from CdS to CdO. It is indeed an oxidation reaction mediated by electron-beam-induced creation of sulfur vacancies. We demonstrate that the oxidation can be greatly suppressed through the deposition of a conductive carbon layer on the surface of the CdS ribbons. This work draws an informative atomic-scale picture on how the oxidation of 1D semiconductor sulfides proceeds and evolves under electron beam stimulation. It may serve as a model experiment for theory to elucidate and predict the irradiation tolerance of 1D sulfides in extreme conditions and provide insights into the mechanisms that lead to aging and degeneration of associated functional materials.

2. Results and discussion

The CdS ribbons employed in this work were synthesized *via* a thermal evaporation process as reported elsewhere[27]. The detailed synthetic procedure is described in the experimental

section. Scanning electron microscopy (SEM) images of CdS ribbons are shown in **Figures 1**a,b. The ribbons are in the wurtzite (WZ) structure (JCPDF 41-1049), as evidenced by X-ray diffraction (XRD, Figure 1c). Scanning transmission electron microscopy (STEM) was also utilized to probe the atomic structure of the ribbons (Figures 1d-f). High-resolution bright-field (BF) STEM shows that the ribbon presents well-resolved lattice fringes with *d*-spacings of 0.34 nm and 0.36 nm, corresponding to the (0002) and (01-10) planes of WZ CdS (Figure 1e). The stacking sequence of ABABAB… along the [0001] orientation matches the atomic model of WZ structure (Figure 1f). Compositional analysis of the ribbon demonstrates that, in addition to Cd and S, a trace amount of oxygen is found at the surface of CdS (Figures 1h-k).

In order to systematically investigate the irradiation effect of CdS ribbon, three different facets, *i.e.*, (01-10), (0001) and (03-31), respectively, were chosen for in-situ observation and identification. It needs to be emphasized that during the entire observations the ribbons were irradiated with a constant electron dose rate of 5330e/Å^{2}s. **Figures 2**a-d show a sequence of high-resolution TEM (HRTEM) images recorded during real-time observation of a CdS (01-10) facet. It is found that upon electron-beam irradiation, the ribbon undergoes significant structural modification at the surface (Movie M1a). The evolution starts first with atomic diffusion at the surface and subsequently, nucleation events take place. Further growth of the nuclei leads to the formation of a new phase on the (01-10) plane of CdS. It is interesting to note that the growth propagates initially outwards, inducing a slight swelling of the surface and only subsequently expands inwards. Besides this behavior, structural defects such as void formation are also observed in the ribbon, which are a result of the agglomeration of mobile vacancies[4]. These voids expand their volumes upon continuous irradiation, causing a gradual thinning of the ribbon. Chemical analysis was performed on the newly grown layer (Figures S1a,b). Energy dispersive X-ray spectroscopy (EDX) shows only Cd and O elements on the side surface of CdS ribbon, due to the presence of CdO. This result is confirmed by the

structural characterization shown in Figure S2. The lattice fringes with *d*-spacings of 0.24 nm correspond to the (002) and (020) planes of a rock salt (RS) structure. It is worth mentioning that the CdO layer grows not only on the side surfaces of the ribbon as presented in Figure 2 but also on the top/down surfaces, which is clearly indicated by the high angle annular dark-field (HAADF) STEM image in Figure S1a. The reason for its "absence" from top/down surfaces in HRTEM mode (Figure 2) lies in the poor phase contrast of CdO arising from its smaller thickness compared to that of the bulk[28]. Interestingly, the grown CdO layer was found to have a crystallographic orientation relationship with the primary CdS, that is, $(01\text{-}10)_{CdS}$ // $(020)_{CdO}$, $[0002]_{CdS}$ // $[002]_{CdO}$ (Figure S2). Due to the lattice mismatch between these two planes (~29%), asymmetric stress is induced in both components, acting as compression in CdS and tension in CdO, respectively. Real-time imaging clearly shows that during the CdO growth, the CdO domains bend slightly towards the outside (Figure S3 and Movie 1a), confirming the existence of stress in the grown CdO. With further growth, the CdO domains free themselves from the bow-like shape as a result of stress releasing. The large-misfit epitaxial growth behavior can be understood by a classic theoretical model, coincidence site lattice (CSL)[29]. The theory is based on a simple assumption that the higher the coincidence of atomic positions has, the lower the grain boundary energy will be. In this case, the d-spacing of five CdS (0002) layers is about 1.70 nm, which is close to that of seven (020) layers of CdO (7×0.24=1.68 nm). The construction along the interface with the periodicity of 5×CdS(0002) and 7×CdS(020) makes the system in a local minimum energy state[30]. The realistic strain in the grown CdO, therefore, is much smaller (~1.2%) compared to the natural misfit between CdS and CdO, thus resulting in an epitaxial growth manner.

The same experimental condition was also used during in-situ observation of polarized CdS (0001) plane (Movie M1b). Several movie frames are selected to show in Figures 2e-h. The growth starts immediately when the ribbon is exposed to the electron beam. Over extended time, the CdO grows in a layer at the CdS (0001) plane. Structural characterization

demonstrates that the present case displays two sets of orientation relationship, they are $(0001)_{CdS}$ // $(002)_{CdO}$, $[01\text{-}10]_{CdS}$ // $[020]_{CdO}$, and $(0001)_{CdS}$ // $(111)_{CdO}$, $[2\text{-}1\text{-}10]_{CdS}$ // $[1\text{-}10]_{CdO}$, as exhibited in Figure S4b,c. Crystallographically speaking, the former is equivalent to that shown in Figure S2 despite the fact that the interfacial plane differs. They are (01-10) and (0001) planes in reference to CdS, respectively. The latter, *i.e.*, $(0001)_{CdS}$ // $(111)_{CdO}$ and $[2\text{-}1\text{-}10]_{CdS}$ // $[1\text{-}10]_{CdO}$, however, is completely different. The appearance of a new orientation relationship is probably due to the common polarity characteristic and the similarity in atomic arrangement between CdS (0001) and CdO (111) planes, as illustrated in Figure S5. In addition, due to the lattice mismatch between the CdO and the CdS, the lattice distortion is also observed during the phase transition.

Finally, the growth kinetics of CdO on a CdS (03-31) facet is represented in Figure 2i-k. Remarkably, the final morphology of the ribbon differs from the one above. It is observed that at the initial stage, the (03-31) surface of ribbon is rather smooth regardless of the nature of high-index plane. During electron-beam irradiation, multiple steps, representing (002) and (020) planes of CdO (some are {111} planes), appear on the surface of the ribbon (Movie M1c). Structural characterization indicates that the orientation relationships between the CdO steps and the CdS are exactly the same as those revealed in Figure 2f, which are $(0001)_{CdS}$ // $(002)_{CdO}$, $[01\text{-}10]_{CdS}$ // $[020]_{CdO}$, and $(0001)_{CdS}$ // $(111)_{CdO}$, $[2\text{-}1\text{-}10]_{CdS}$ // $[1\text{-}10]_{CdO}$, respectively (Figure S6). The identical orientation relations in these two cases are due to the same interfacial plane, *i.e.*, (0001) plane in reference of CdS. The presence of stepped surface can probably be determined by a Wulff construction[31], as it is likely driven by the tendency to minimize the total surface energy of the system through forming low surface energy planes[32].

In order to quantify the growth kinetics, we plotted the cumulative thickness of the CdO grown on (01-10), (0001) and (03-31) planes, as shown in Figure 2l. One can see that the shape and trend of these curves are similar, indicating that the CdO growth on different planes

follows similar kinetic behavior. The final thickness of CdO is also found to be in close proximity in all cases (~3.5 nm). Figure 2m shows the growth speed of CdO as a function of irradiation time, which is derived from Figure 2l. Two distinct growth stages are identified. Stage I represents a fast growth period during which the growth speed is increasing. In stage II, however, the CdO growth speed starts to decrease. It seems that the transition from CdS to CdO is inhibited by the already transformed oxide layer, signifying a diffusion-limited growth[33]. To summarize, real-time observations reveal that an electron beam can stimulate a structural transition from CdS to CdO at the surface. The formed CdO shows facet-dependent orientation relationships with the primary CdS. Our observations indicate that the CdO growth at different facets shows a similar evolution pattern.

So far we have discussed the irradiation induced transformation under a constant electron beam dose rate. In the following, we investigate the dose rate dependence of the process. **Figure 3**a-f shows a sequence of HRTEM images recorded during real-time observation of the (0001) facet of a [2-1-10] oriented CdS ribbon upon exposure to 2360, 1200, and 601 e/Å^{2}s, respectively. It is found that the transition from CdS to CdO can proceed under all three conditions (Movie M2a,b,c) and leads to an oxide layer with a thickness of ~3.5 nm. Although our kinetic study reveals that the growth behavior is not influenced by the dose rate (Figure S7), it seems that the crystalline order of the formed CdO increases from 601 to 2360 e/Å^{2}s. In the next step, the dose rate was decreased to 311 e/Å^{2}s in order to look for a lower threshold. Under low dose irradiation, the formation of an amorphous carbon layer on the CdS was observed instead of CdO growth (Figures 3g,h, Move M3a). Carbon deposition is caused by the cracking of carbon species at the sample surface upon irradiation. This phenomenon is frequently observed during SEM or TEM characterizations due to carbon contamination[14]. The carbon species generally originates from contamination of the sample surface but can also be due to residual gas in the TEM vacuum chamber. After protection of the surface by the

carbon layer, both structural damage and CdO formation are prevented (Figures 3g,h). Indeed, the structure barely shows any change after approximately 11 minutes of irradiation. We then increased the electron dose rate to 2380 e/Å^{2}s. One can see that during the first 5 minutes, the carbon layer remains complete and no observable damage occurs on the covered CdS (Figures 3i,j, Movie M3b). However, after 10 minutes of irradiation, the carbon layer starts to develop pores. Once the pores are formed, the structural transition of CdS to CdO is initiated (Figure 3j and Movie M3b). To speed up the process, we further increased the dose rate to 5390 e/Å^{2}s (Figures 3k,l, Movie M3c). At this high dose rate, the surface carbon layer is etched faster and layer-by-layer growth of CdO is observed (Figure S8). Structure analysis confirms that the formed atomic layers are (002) planes of CdO. In order to confirm the protective action of the carbon layer, an even thicker layer (~25 nm) was deposited on a region not previously exposed to the electron beam. As before, no transformation of CdS to CdO was observed even at an electron dose rate of 5240 e/Å^{2}s and irradiation up to 655s (Figure S9, Movie M4).

In the following, we try to address the origin of the oxygen. The presence of trace amounts of oxygen on the surface of the nanoribbons was confirmed by EDX. They could contribute to the formation of CdO. However, previous work also points out that the oxygen species in the column of the TEM can participate in reactions under beam stimulation[34, 35]. In order to examine whether the phase transition involves oxygen species from the gas phase or the surface of the ribbons, an in-situ heating experiment was performed inside the TEM using a MEMS (**Figure 4**a) based heating holder (Figure S10). Heating in vacuum in the absence of the beam should lead to the desorption of adsorbed oxygen species. After heating at 300°C for 30 min, the beam was turned on and the ribbon exposed to a dose rate of 6480 e/Å^{2}s. Figures 4c-e show a series of HRTEM images recorded during in-situ observation of the ribbon at 300°C. Although structural damage is observed, no CdO formation could be observed (Movie M5). The inhibition of the phase transition indicates that the primary source of oxygen on the

surface of the ribbons desorbed upon heating. Next, we dropped the temperature to 23°C. Time-resolved HRTEM images recorded at the same region are shown in Figures 4f-h. It is found that after the temperature drops the phase transition is initiated (Movie M5). Structural characterization (insets of Figure 4h) confirms that the newly generated structures are CdO. Since the chemisorbed oxygen has been removed by the pre-treatment, it is reasonable to speculate that the residual gas in the TEM (around 10^{-6} Pa) contains a sufficient amount of oxygen that can be activated by the electron beam and induce the structural transition.

In-situ electron energy loss spectroscopy (EELS) was also employed to study the transition of CdS to CdO. **Figure 5**a shows a series of time-course EELS spectra recorded during in-situ scanning TEM (STEM) observation (Figures 5c-e). Figure 5b shows the enlarged portion of energy range indicated by dashed rectangle in Figure 5a. Each presented EELS spectrum is a sum of all EELS spectra recorded in one line profile (indicated by the green line). Initially, the EELS spectrum (0 s) shows a clear sulfur L-edge and the absence of an oxygen K-edge. Under the beam irradiation, the sulfur L-edge gradually fades and becomes less characteristic, indicating loss of sulfur, which is also confirmed by the formation of voids seen in the HAADF images (Figures 5c-e). On the contrary, the oxygen K-edge appears and grows progressively over time, suggesting the formation of CdO. This result coincides well with the above in-situ TEM observations, and confirms that the CdO is formed through the replacement of sulfur by oxygen.

To test if oxide growth is expected, we explored how the stability of a CdO layer on CdS changes as a function of oxide thickness by way of density functional theory calculations. For complete details of the approach see the methods section. Briefly, we employed an 8-layer (01-10) CdS surface. We then adsorbed 1, 2, or 8-layers of CdO with a (020) surface termination on the CdS slab. To minimize lattice mismatch, a (4x1) supercell of CdS was employed with a (5x2) supercell of CdO (**Figures 6**a-c). The in-plane dimensions of the CdS

surface were fixed at their computed values (16.76 Å x 6.83 Å). Thus a ~2% compression of the CdO lattice was required to make it commensurate with the CdS surface. We then define the average oxygen substitution energy as:

$$\langle E_{sub} \rangle = \frac{1}{N}\left(E_{CdS/CdO} - E_{CdS} - \frac{N}{2}E_{O_2} - N\,E_{Cd}\right), \qquad (1)$$

where $E_{CdS/CdO}$ (E_{CdS}) is the total energy of the CdS surface with (without) adsorbed CdO, N is the number of CdO formula units in the CdO layer(s), E_{Cd} is the total energy of a Cd atom in the bulk metal, and E_{O_2} is the total energy of O_2. Using this definition we found that the average oxygen substitution energy rapidly becomes more exothermic with increasing CdO thickness, dropping from -0.43 eV for a single oxygen atom to -1.62 eV/O for 1-layer of CdO, -1.86 eV/O for 2-layers of CdO, and -1.98 eV/O for 8 layers of CdO. While this shows oxygen substitution can be exothermic when the beam introduces S vacancies, it does not indicate if the process is spontaneous.

To compute the free energy changes associated with oxide growth we employ *ab initio* atomistic thermodynamics[36] by replacing their total energies of O_2 and Cd in equation 1 by the corresponding chemical potentials to yield the change surface free energy associated with CdO growth on CdS:

$$\Delta\gamma(T,p) \sim \frac{1}{A}\left(E_{CdS/CdO} - E_{CdS} - \frac{N}{2}\mu_{O_2} - N\,\mu_{Cd}\right), \qquad (2)$$

where A is the surface area of the slab, μ_{O_2} is the chemical potential of gas phase O_2, and μ_{Cd} is the chemical potential of Cd. By assuming the total energies of the solid phases are independent of (T,p) and the chemical potential of Cd is the total energy of Cd in its thermodynamic reservoir, CdS or Cd metal, the pressure and temperature dependence of the free energy can be captured by μ_{O_2} alone. The oxygen chemical potential can then be written as the total energy of an O_2 molecule with a (T,p) dependent entropic correction[36]. While neglecting entropic contributions for the CdO overlayer will tend to lead to an error in the

temperature at which its growth is spontaneous, for other systems this error is often small (~100 K)[36-38].

The surface free energies computed using equation 2 are shown in Figure 6d as a function of $\Delta\mu_O$, $\frac{1}{2}(\mu_{O_2} - E_{O_2})$. Here the solid lines show $\Delta\gamma(T,p)$ computed using Cd metal for μ_{Cd} whereas the dashed lines show the $\Delta\gamma(T,p)$ when μ_{Cd} is taken as Cd in CdS. Inspection of the figure reveals that under conditions where the Cd chemical potential is near that of Cd metal growth of the thin layers of CdO on CdS considered here is spontaneous down to $\Delta\mu_O \sim -2\ eV$, which is the oxygen chemical potential at roughly 900 K at 10^{-12} bar O_2 pressure. Conversely, if μ_{Cd} is fixed by CdS, that is $\mu_{Cd} = E_{CdS} - E_{Cd}$, the growth of a thin CdO surface oxide is only predicted to be spontaneous down to $\Delta\mu_O \sim -0.2\ eV$, or ~100 K at 10^{-12} bar O_2 pressure. Thus, we conclude that when excess Cd is present due to the beam damage, and S vacancy formation, CdO growth will be thermodynamically favorable over a wide range of oxygen chemical potentials, even those likely present in the TEM chamber.

On the basis of the experimental results and DFT calculations, a mechanism for the phase transition is proposed (**Figure 7**). Beam induced knock-on damage as well as radiolysis can give rise to displacement of sulfur atoms from the CdS lattice and the generation of S vacancies (Figure 7b). The vacancies are either very mobile or induce local destabilization of the lattice, which lowers the barrier for the formation of further vacancies[39]. Consequently, clustering of point defects occurs, giving rise to the observed void formation. In parallel to this process, the oxygen source in the TEM column, which maybe water or molecular oxygen, is ionized and dissociated by the electron beam, resulting in the formation of highly reactive oxygen radicals (Figure 7b). Subsequently, the large potential difference drives these oxygen radicals into the vacancy sites and leads to the formation of CdO species within the CdS crystal lattice (Figure 7c). Since the structure of CdO is incompatible with that of CdS, the formed CdO species diffuse towards the surface (Figure 7d). With time, the aggregation of

CdO species leads to formation of an oxide layer at the surface (Figure 7e). The kinetic study of the oxidation process shown in Figure 2l reveals that the growth speed of the oxide varies with time. It increases sharply during the first 100-150s and drops slowly for the remaining observation time. We think that the initial oxidation is determined by a surface-kinetic process[40] due to the low diffusion barrier of oxygen, thus showing a fast growth rate of CdO. Strain at the interface between the expanding oxide layer and the sulfide induces further defects and accelerates the oxidation during the initial phase. With growing thickness of the oxide layer, however, diffusion processes through that layer start slowing down the process and finally, lead to a self-limited growth behavior. The oxidation process described here differs from thermal oxidation[30] in that it proceeds at room temperature and it is driven by electron-beam irradiation instead of thermal heating. We assume that the sulfur vacancies play a vital role in the observed CdS oxidation. The process is clearly related to the action of the beam, since nearby regions that have not been exposed to high-energy electrons do not show any modifications (Figure S11). We consider that the energy barrier for the oxygen radicals to directly replace the sulfur is too high to make that process likely. On the other hand, electron-beam-induced formation of sulfur vacancies significantly lowers the reaction barrier, making the oxidation reaction a thermodynamically favorable process. We also demonstrate that the above described irradiation-induced oxidation can be strongly suppressed by covering the surface of the CdS ribbon with a carbon layer (Figure S9). It prevents charging and acts as a reservoir of electrons[5], thus minimizing the generation of sulfur vacancies through radiolysis. Secondly, it prevents the diffusion of oxygen radicals towards sulfur vacancies in the CdS.

3. Conclusion

In summary, this work presents real-time observation of irradiation induced structural modifications. Using CdS as a model system, we show that electron beam is able to stimulate the formation of CdO in CdS surface. Facet-dependent orientation relationships are explored between the growing oxide layer and the bulk CdS structure. Furthermore, the effect of dose

rate was investigated. It revealed that the phase transition can be triggered by a dose rate above 601 e/Å^{2}s, while a lower dose rate, leads to deposition of an amorphous carbon layer on the surface of the CdS which prevents oxidation towards CdO. On the basis of the observed behavior and DFT calculations, a mechanism for the phase transition was proposed. It is essentially a thermodynamically driven process assisted by the electron beam irradiation. Irradiation of the sample with the electron beam leads to creation of sulfur vacancies on one hand, and ionization and disassociation of oxygen species that are present at the surface of the ribbons and in the column of the microscope on the other. The diffusion of oxygen radicals into the sulfur vacancies is driven by a potential gradient. Aggregation of CdO species results in growth of CdO at the surface of the CdS ribbons. It is also shown that the irradiation-stimulated oxidation process can be strongly inhibited by depositing a conductive carbon layer on the surface of the CdS. The carbon layer effectively reduces the rate of sulfur vacancy generation, thus reducing the driving force for the oxygen diffusion. At the same time, it isolates the active oxygen radicals from the ribbon, blocking the pathway of oxygen diffusion to the vacancies. Our work provides an insight on electron-beam-stimulated oxidation process, and provides an effective method for the reduction of beam damage.

Experimental Section

Synthesis of CdS ribbon. The CdS ribbon is synthesized through a thermal evaporation method performed in a high temperature tube furnace. Analytically pure CdS powder was put into a ceramic boat which was then located at the heating zone of the furnace. A piece of silicon wafer was put downstream 5 cm away from the boat. After the furnace was sealed, the tube in the furnace was evacuated. After the pressure inside reached to 0.1 Pa, a constant air flow of 45 sccm (standard cubic centimeters per minute) was flowed into the tube. The pressure of the system was kept at 80 Pa. Then the powder was heated up to 850°C within 25

minutes and maintained at the temperature for 30 minutes. After that, the furnace was cooled down to room temperature and CdS ribbons were grown on the Si wafer.

Characterization. SEM images were taken on a Hitachi S-4800 SEM operated at an accelerate voltage of 10 kV. In-situ observations were performed in an FEI 80-300 abreaction-corrected transmission electron microscope (TEM) operated at 300 kV under different dose rates. The TEM was equipped with an EDX detector which allows for chemical analysis. In-situ heating experiment in the microscope was performed with a TEM heating holder purchased from DENSsolutions. The holder is mounted with a heating chip which serves as a sample carrier. In-situ STEM-EELS experiment was carried out on an abreaction-corrected JEOL JEM-ARM200F TEM equipped with a GIF Quantum energy filter. Dual EELS mode was applied to record the low loss and high loss spectra spontaneously.

DFT calculation. The Quantum ESPRESSO package[41] was used for density functional theory (DFT) calculations, which were performed with the Perdew, Burke, and Ernzerhof (PBE) approximation for the exchange and correlation potential[42]. Ultrasoft pseudopotentials taken from the PS library[43], and a plane-wave basis set with a kinetic energy (charge density) cutoff of 30 Ry (300 Ry) was employed. A **k**-point mesh of at least to (16x8) was used for the (1x1) surface unit-cell along with Marzari-Vanderbilt cold smearing with a smearing parameter of 0.001 Ry[44]. Surfaces for the vacancy calculations were modeled with (2x2) 8 layer slabs with the bottom 3 layers fixed at their computed bulk values (a=4.19 Å, c=6.83 Å). The CdO/CdS surfaces were treated with an equivalent **k**-point mesh with the bottom 3 layers of the CdS slabs fixed and the geometry described in the main text. The computed bulk lattice parameter of CdO was 4.74 Å.

For adsorption energy calculations the oxygen reservoir was considered to be O_2 and the sulfur reservoir gamma-sulfur. The total energy of oxygen was taken from a calculation on an O_2 molecule at the Γ point using a box whose side lengths were approximately 25 Å. The energy of sulfur was taken as the total energy of an atom in gamma-sulfur[45] where the

measured lattice parameters and atomic positions were used and the calculation was performed on a (8x8x8) **k**-point mesh. For *ab initio* atomistic thermodynamics calculations[36] the entropic correction for the gas phase chemical potential of O_2 was taken from the NIST JANAF thermochemical tables[46].

Supporting Information
Supporting Information is available from the Wiley Online Library or from the author.

Acknowledgements
We thank Dr. Gerardo Algara-Siller, Dr. Elena Willinger and Dr. Detre Teschner for valuable discussions. We gratefully acknowledge Höchst-Leistungs-Rechensentrum Stuttgart (HLRS) for generous access to the supercomputer HazelHen. T. E. J. acknowledges the Alexander-von-Humboldt foundation for financial support.

Received: ((will be filled in by the editorial staff))
Revised: ((will be filled in by the editorial staff))
Published online: ((will be filled in by the editorial staff))

References

[1] X. H. Zhao, Z. G. Shen, Y. S. Xing, S. L. Ma, *Polym. Degrad. Stabil.,* 2005, **88**, 275-285.
[2] R. W. Grimes, R. J. M. Konings, L. Edwards, *Nat. Mater.,* 2008, **7**, 683-685.
[3] R. W. Hamm, M. E. Hamm, *Phys. Today,* 2011, **64**, 46-51.
[4] W. Z. Xu, Y. F. Zhang, G. M. Cheng, W. W. Jian, P. C. Millett, C. C. Koch, S. N. Mathaudhu, Y. T. Zhu, *Nat. Commun.,* 2013, **4**, 6.
[5] G. Algara-Siller, S. Kurasch, M. Sedighi, O. Lehtinen, U. Kaiser, *Appl. Phys. Lett.,* 2013, **103**, 5.
[6] S. Takeda, *Jpn. J. Appl. Phys. Part 2 - Lett.,* 1991, **30**, L639-L642.
[7] D. GomezGarcia, J. MartinezFernandez, A. DominguezRodriguez, K. H. Westmacott, *J. Am. Ceram. Soc.,* 1996, **79**, 2733-2738.
[8] C. Karthik, J. Kane, D. P. Butt, W. E. Windes, R. Ubic, *J. Nucl. Mater.,* 2011, **412**, 321-326.
[9] L. D. Yao, S. Majumdar, L. Akaslompolo, S. Inkinen, Q. H. Qin, S. van Dijken, *Adv. Mater.,* 2014, **26**, 2789-2793.
[10] R. A. Andrievskii, *Phys. Metals Metallogr.,* 2010, **110**, 229-240.
[11] N. Thangaraj, B. W. Wessels, *J. Appl. Phys.,* 1990, **67**, 1535-1541.
[12] I. J. Beyerlein, A. Caro, M. J. Demkowicz, N. A. Mara, A. Misra, B. P. Uberuaga, *Mater. Today,* 2013, **16**, 443-449.
[13] J. Kotakoski, A. V. Krasheninnikov, U. Kaiser, J. C. Meyer, *Phys. Rev. Lett.,* 2011, **106**, 4.
[14] R. F. Egerton, P. Li, M. Malac, *Micron,* 2004, **35**, 399-409.
[15] S. R. Singh, L. D. Marks, *Philos. Mag. Lett.,* 1989, **60**, 31-36.
[16] J. W. Wang, Z. Zeng, C. R. Weinberger, Z. Zhang, T. Zhu, S. X. Mao, *Nat. Mater.,* 2015, **14**, 594-600.
[17] W. T. Yuan, Y. Wang, H. B. Li, H. L. Wu, Z. Zhang, A. Selloni, C. H. Sun, *Nano Lett.,* 2016, **16**, 132-137.
[18] Z. Zhang, Y. Wang, H. Li, W. Yuan, X. Zhang, C. Sun, Z. Zhang, *ACS Nano,* 2016, **10**, 763-769.
[19] A. V. Krasheninnikov, K. Nordlund, *J. Appl. Phys.,* 2010, **107**, 70.
[20] B. L. Cao, Y. Jiang, C. Wang, W. H. Wang, L. Z. Wang, M. Niu, W. J. Zhang, Y. Q. Li, S. T. Lee, *Adv. Funct. Mater.,* 2007, **17**, 1501-1506.
[21] A. L. Pan, D. Liu, R. B. Liu, F. F. Wang, X. Zhu, B. S. Zou, *Small,* 2005, **1**, 980-983.
[22] Y. F. Lin, J. Song, Y. Ding, S. Y. Lu, Z. L. Wang, *Appl. Phys. Lett.,* 2008, **92**, 3.

[23] H. M. Fan, Z. H. Ni, Y. P. Feng, X. F. Fan, J. L. Kuo, Z. X. Shen, B. S. Zou, *Appl. Phys. Lett.,* 2007, **91**, 3.
[24] D. H. Li, J. Zhang, Q. Zhang, Q. H. Xiong, *Nano Lett.,* 2012, **12**, 2993-2999.
[25] J. S. Jang, U. A. Joshi, J. S. Lee, *J. Phys. Chem. C,* 2007, **111**, 13280-13287.
[26] H. Choi, P. V. Kamat, *J. Phys. Chem. Lett.,* 2013, **4**, 3983-3991.
[27] J. S. Jie, W. J. Zhang, Y. Jiang, X. M. Meng, Y. Q. Li, S. T. Lee, *Nano Lett.,* 2006, **6**, 1887-1892.
[28] A. S. Masadeh, E. S. Bozin, C. L. Farrow, G. Paglia, P. Juhas, S. J. L. Billinge, A. Karkamkar, M. G. Kanatzidis, *Phys. Rev. B,* 2007, **76**, 11.
[29] M. L. Kronberg, F. H. Wilson, *Transactions of the American Institute of Mining and Metallurgical Engineers,* 1949, **185**, 501-514.
[30] G. W. Zhou, L. L. Luo, L. Li, J. Ciston, E. A. Stach, J. C. Yang, *Phys. Rev. Lett.,* 2012, **109**, 5.
[31] G. Wulff, *Z Krystallogr. Mineral,* 1901, **34**, 449-530.
[32] J. I. Sohn, W. K. Hong, S. Lee, S. Lee, J. Ku, Y. J. Park, J. Hong, S. Hwang, K. H. Park, J. H. Warner, S. Cha, J. M. Kim, *Sci Rep,* 2014, **4**, 7.
[33] H. Q. Nie, M. Schoenitz, E. L. Dreizin, *J. Phys. Chem. C,* 2016, **120**, 974-983.
[34] T. Wada, *Appl. Phys. Lett.,* 1988, **52**, 1056-1058.
[35] C. M. Wang, D. R. Baer, J. E. Amonette, M. H. Engelhard, J. J. Antony, Y. Qiang, *Ultramicroscopy,* 2007, **108**, 43-51.
[36] K. Reuter, M. Scheffler, *Phys. Rev. B,* 2002, **65**, 11.
[37] A. Soon, M. Todorova, B. Delley, C. Stampfl, *Phys. Rev. B,* 2007, **75**, 9.
[38] T. E. Jones, T. C. R. Rocha, A. Knop-Gericke, C. Stampfl, R. Schlogl, S. Piccinin, *Phys. Chem. Chem. Phys.,* 2015, **17**, 9288-9312.
[39] R. S. Barnes, *Discussions of the Faraday Society,* 1961, 31, 38-44.
[40] L. L. Luo, L. F. Zou, D. K. Schreiber, M. J. Olszta, D. R. Baer, S. M. Bruemmer, G. W. Zhou, C. M. Wang, *Chem. Commun.,* 2016, **52**, 3300-3303.
[41] P. Giannozzi, S. Baroni, N. Bonini, M. Calandra, R. Car, C. Cavazzoni, D. Ceresoli, G. L. Chiarotti, M. Cococcioni, I. Dabo, A. Dal Corso, S. de Gironcoli, S. Fabris, G. Fratesi, R. Gebauer, U. Gerstmann, C. Gougoussis, A. Kokalj, M. Lazzeri, L. Martin-Samos, N. Marzari, F. Mauri, R. Mazzarello, S. Paolini, A. Pasquarello, L. Paulatto, C. Sbraccia, S. Scandolo, G. Sclauzero, A. P. Seitsonen, A. Smogunov, P. Umari, R. M. Wentzcovitch, *J. Phys.-Condes. Matter,* 2009, **21**, 19.
[42] J. P. Perdew, K. Burke, M. Ernzerhof, *Phys. Rev. Lett.,* 1996, **77**, 3865-3868.
[43] A. Dal Corso, *Comput. Mater. Sci.,* 2014, **95**, 337-350.
[44] N. Marzari, D. Vanderbilt, A. De Vita, M. C. Payne, *Phys. Rev. Lett.,* 1999, **82**, 3296-3299.
[45] A. C. Gallacher, A. A. Pinkerton, *Acta Crystallogr. Sect. C-Cryst. Struct. Commun.,* 1993, **49**, 125-126.
[46] M. W. Chase, *NIST-JANAF Thermochemical Tables*. American Chemical Society: New York, 1998.

Figures and captions

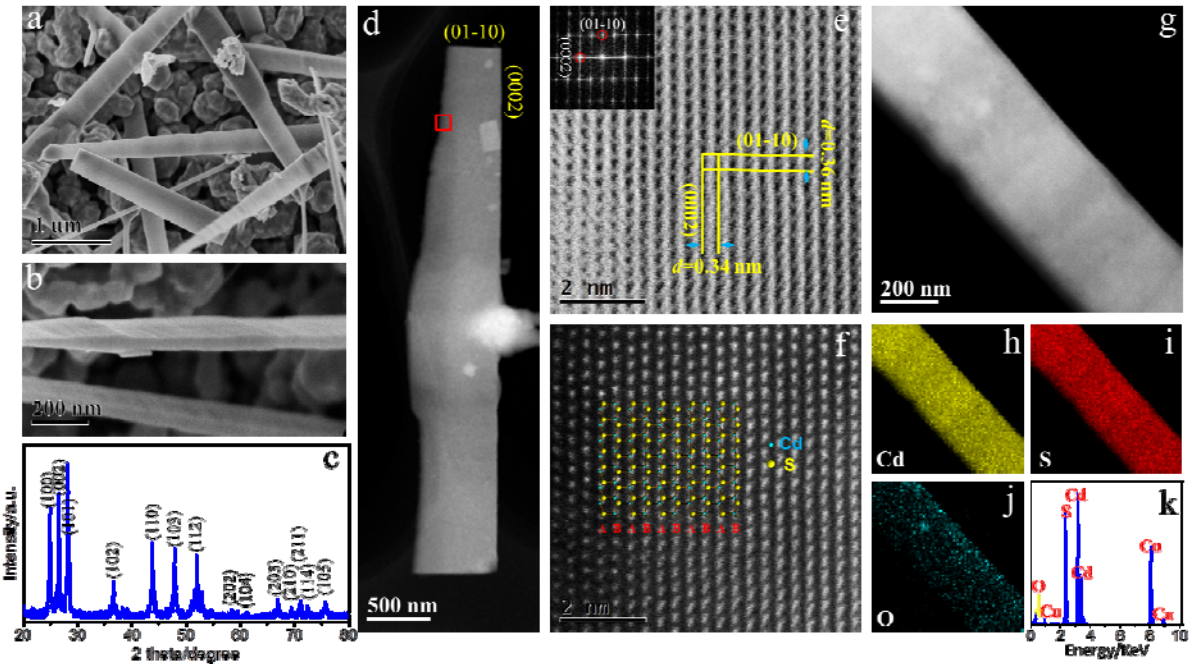

Figure 1. (a,b) SEM images of prepared CdS ribbons at different magnifications; (c) XRD spectrum of CdS; (d) Annular dark-field (ADF) STEM image of a CdS ribbon; (e-f) High-resolution BF-STEM and ADF-STEM images of the CdS ribbon; (g-k) ADF-STEM image and corresponding EDX analysis of a CdS ribbon.

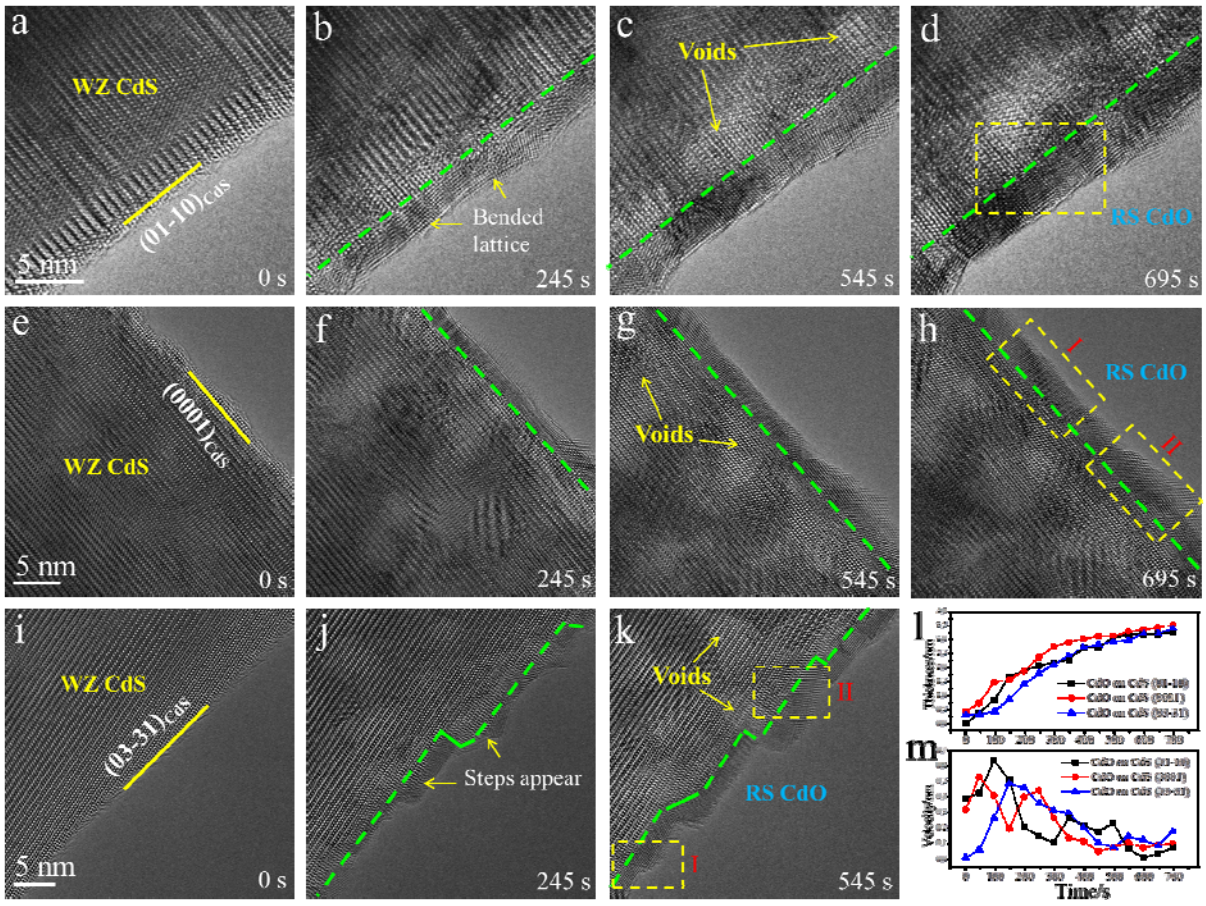

Figure 2. A series of HRTEM images captured during in-situ observation of CdS ribbons under a continuous electron beam irradiation with a constant dose rate of 5330e/Å^{2}s, showing a structure evolution from CdS to CdO; (a-d) (01-10) plane of CdS ribbon; (e-h) (0001) plane of CdS ribbon; (i-k) (03-31) plane of CdS ribbon; (l,m) Thickness and speed of the grown CdO as a function of irradiation time. Green dashed lines indicate the interface between the CdS and the growing CdO. Regions marked with yellow dashed rectangles in Figure 2d, h and k are used for structural analysis (See Figure S2, S4 and S6 for details).

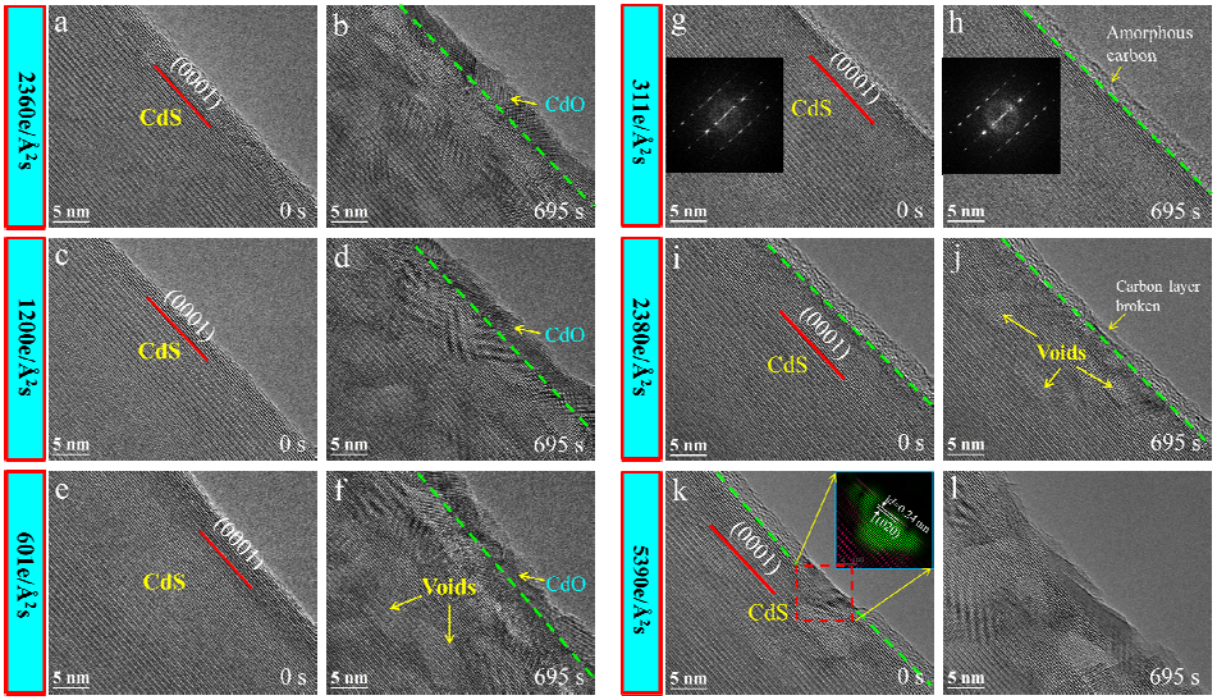

Figure 3. A series of HRTEM images of CdS ribbon under the electron beam with diverse dose rates of (a,b) 2360 e/Å^{2}s, (c,d) 1200 e/Å^{2}s, (e,f) 601 e/Å^{2}s, (g,h) 311 e/Å^{2}s, (i,j) 2380 e/Å^{2}s and (k,l) 5390 e/Å^{2}s, respectively. Green dashed lines indicate the interface between the CdS and the growing CdO. Yellow dashed lines indicate the interface between the CdS and the growing carbon layer.

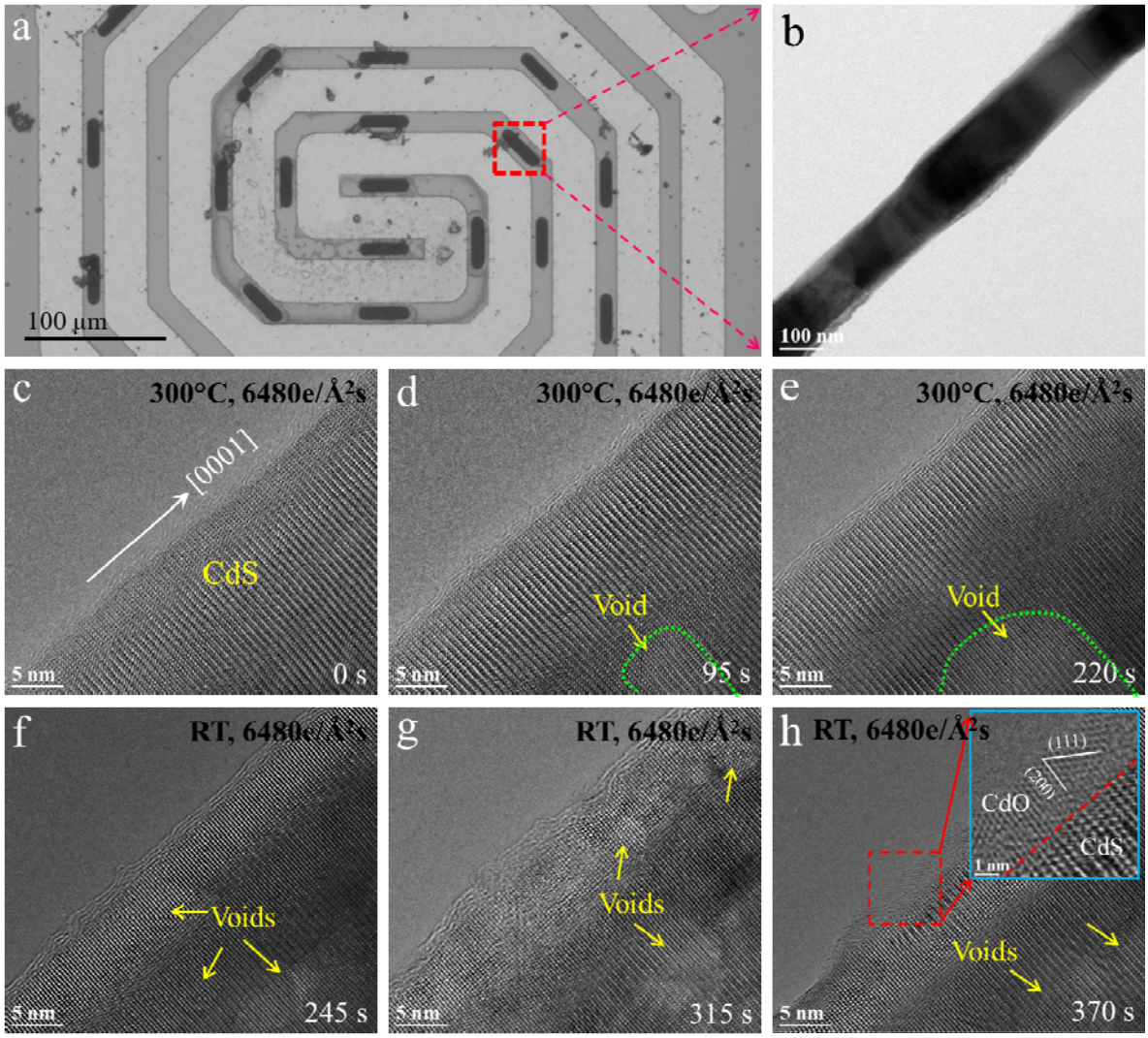

Figure 4. (a) Optical image of a heating chip; (b) TEM image of a CdS ribbon as the object for heating. (c-e) HRTEM images recorded during in-situ observation of the CdS ribbon under a dose rate of 6480 e/Å^{2}s at 300°C; (f-h) HRTEM images recorded during in-situ observation under a dose rate of 6480 e/Å^{2}s at room temperature. Inset of Figure 4h shows an enlarged HRTEM image taken from the interfacial region; the red dashed line indicates the interface between the CdO and the CdS.

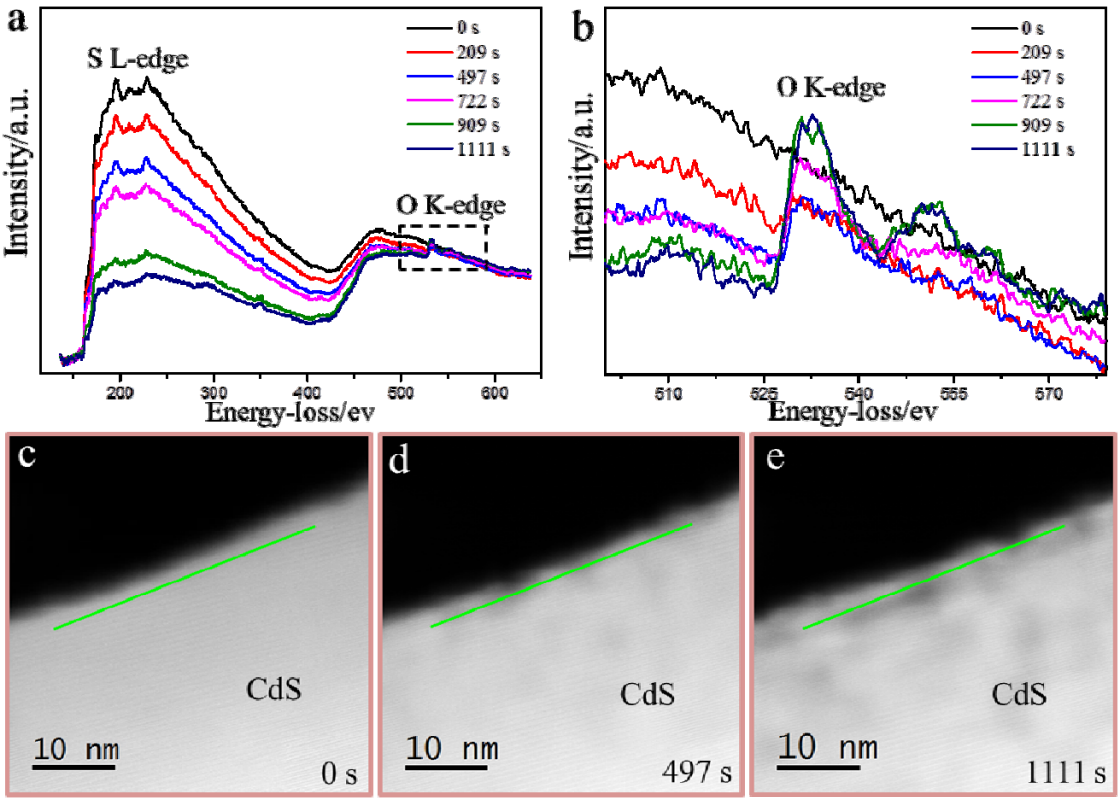

Figure 5. In-situ EELS analysis. (a) Time-resolved EELS spectra of a CdS ribbon recorded in STEM mode along the green line; (b) EELS spectra taken from the rectangle region labeled in Figure 6a; (c-e) series of ADF-STEM images showing the structure evolution of CdS ribbon.

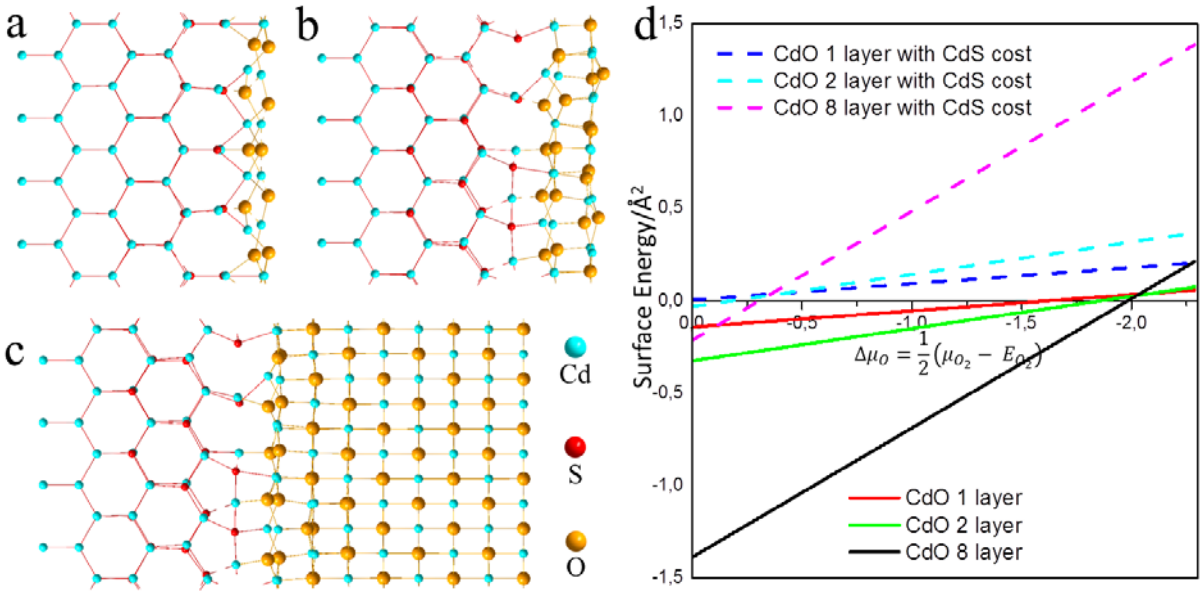

Figure 6. (a-c) Atomic models of 1, 2, or 8-layers of CdO with a (020) surface termination on the CdS (01-10) surface; (d) Plot of the change in surface free energy associated with CdO growth on a CdS surface as a function of $\Delta\mu_O = \frac{1}{2}(\mu_{O_2} - E_{O_2})$. The solid lines show the results obtained when assuming the Cd chemical potential in the CdO overlayer is fixed by Cd metal. The dashed lines shows the result when $\mu_{Cd} = E_{CdS} - E_{Cd}$.

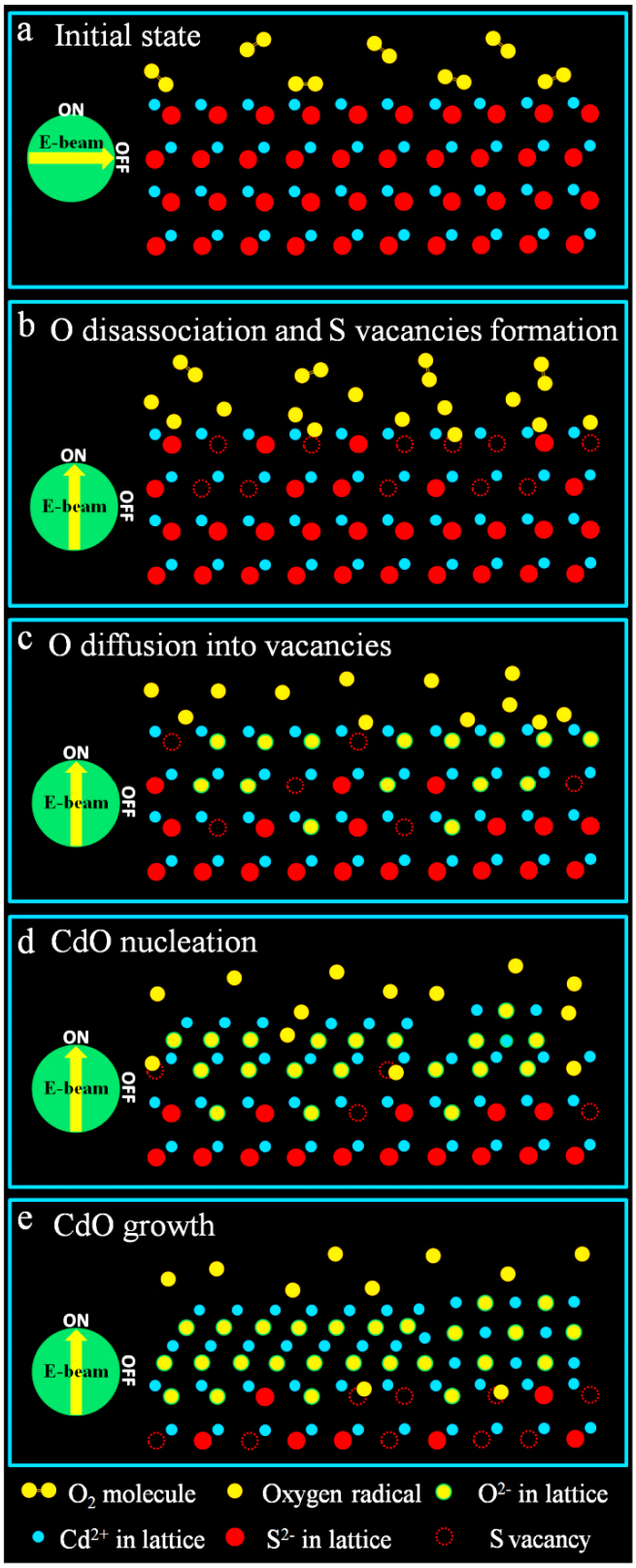

Figure 7. Atomic modes, showing the oxidation mechanism of CdS under the electron beam irradiation. In this model, we use O_2 to represent the oxygen species in the TEM column.

TOC figure

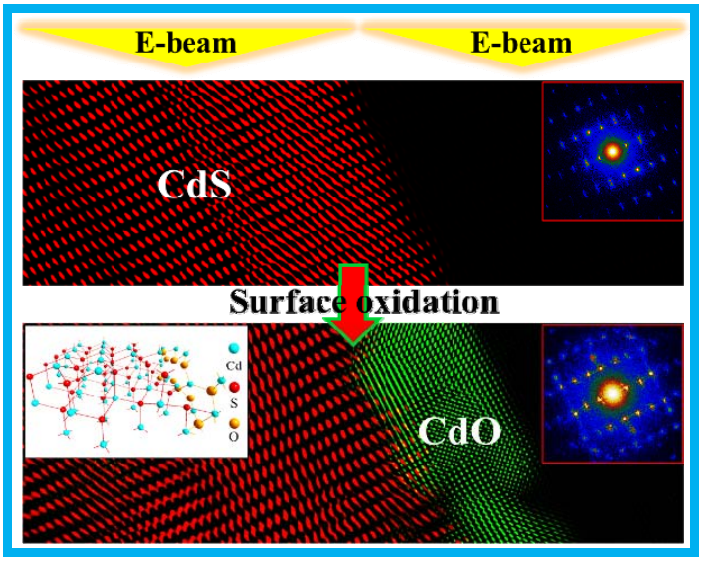

Electron-beam irradiation induced structural transition has been systematically studied by real-time transmission electron microscopy. Our result shows that upon irradiation CdS is transformed to CdO at the surface. Combined with real-time observation and DFT calculations, we demonstrate that the transition is essentially a thermodynamically driven process which is mediated by the formation of sulfur vacancies induced by electron-beam irradiation.

Keyword in-situ TEM, EELS, electron-beam irradiation, structural transition, sulfur vancancy